

Estimating energy input rate from vertical profiles of energy dissipation rate

Nozomi Sugiura^{1,*}, Shinya Kouketsu¹, Shuhei Masuda¹, Satoshi Osafune¹, and Ichiro Yasuda²

¹Research and Development Center for Global Change, JAMSTEC, Yokosuka, Japan

²Atmosphere and Ocean Research Institute, University of Tokyo, Chiba, Japan

*nsugiura@jamstec.go.jp

ABSTRACT

The energy dissipation rate is an important characteristic of turbulence; however, its magnitude in observational profiles can be misidentified owing to its erratic evolution. By analysing observed data from oceanic turbulence, we show that the vertical sequences of depth-averaged energy dissipation rates have a scaling property. Subsequently, we propose a method to estimate the energy input rate by utilising this property. For scaling in the observed profiles, we show that our data have a statistical property that is consistent with the universal multifractal model, which comprises α -stable generators with parameters $\alpha = 1.74$ and $C_1 = 0.393$. Meanwhile, the energy input rate and its uncertainty given observation can be estimated by inverting the probability distribution obtained by Monte Carlo simulations of the cascade model, through imposing observational constraint from several moments over each vertical sequence.

Introduction

The importance of determining the energy dissipation rate to study ocean general circulation has been highlighted in numerous studies^{1,2}. Hence, a large number of observational studies have been conducted to obtain the vertical profiles of the energy dissipation rate using ocean microstructure profilers^{3,4}. In addition, to understand the statistics of the erratic evolution of observational profiles, studies have been conducted from the viewpoint of statistical fluid mechanics, as summarised below.

In fully developed turbulence, there exists an inertial subrange where the advective term is dominant over the molecular viscosity term in the Navier–Stokes equation⁵. In the inertial subrange, there is a cascade of energy from large to small, as intuitively stated by Richardson⁶. As the first quantitative theory on the energy cascade, Kolmogorov⁷ established a relationship wherein velocity fluctuations are locally isotropic and are determined by the homogeneous energy dissipation rate,

$$\langle |v(x+\ell) - v(x)| \rangle \approx \varepsilon^{1/3} \ell^{1/3}, \quad (1)$$

where $\langle \cdot \rangle$ denotes the ensemble average. Subsequently, it was argued that the energy dissipation rate is not only homogeneous, but also shows significant random fluctuations⁸. A refined theory was thus proposed to address this issue⁹. The theory stated that i) $\log \varepsilon_r$, which is the logarithm of the spatially averaged energy dissipation rate over scale r , obeys a Gaussian distribution, and ii) its variance obeys $\sigma_{\log \varepsilon_r}^2 = A + \mu \log(L/r)$ (L : the outer scale).

Additionally, several experimental studies^{10,11} showed that small-scale dissipation is a random field that has a spatial structure with power-law correlations,

$$\langle \varepsilon(x)\varepsilon(x+\ell) \rangle \propto \ell^{-\mu}. \quad (2)$$

Then, Yaglom¹² formulated a quantitative model, which was consistent with the scaling log-normality and the power-law correlations, as a multiplicative cascade, where ε_r was expressed with a binary tree composed of i.i.d random variables, $W_{i,k}$ ($\sim W$),

$$\forall 1 \leq j \leq 2^n, \quad \varepsilon_r(x_j) = \prod_{i=1}^n W_{i,[(j-1)/2^{n-i}]+1}, \quad (3)$$

where $[\cdot]$ is the Gauss symbol. If the random variables are set to have the moment exponent, $K(q) = \log_2 \langle W^q \rangle = (\mu/2)(q^2 - q)$, then the energy conservation and the log-normality at each scale in Kolmogorov (1962)⁹ are reproduced. Moreover, correlation (2) is reproduced because we have $\langle \varepsilon(x)\varepsilon(x+\ell) \rangle = \langle W^2 \rangle^{n-m} \langle W \rangle^{2m} \propto \ell^{-K(2)}$, where $L = 2^n r$, $\ell = 2^m r$ for small r ^{12,13}.

There have been several alternative multiplicative cascade models with different generators, including the β -model¹⁴, random β -model¹⁵, α -model¹⁶, p -model¹⁷, log-stable model¹⁸, and log-Poisson model¹⁹. An important observation regarding Yaglom's cascade is that the property required for the law of random variable W can be abstracted such that the product of several random variables still obeys the same class of distribution, $\prod_{i=1}^n W_i \sim a_n W^{b_n}$, with $a_n, b_n > 0$ ²⁰. Consistent with this condition, the universal multifractal model¹⁸ employs a stable Lévy generator, Γ , that is maximally left skewed, and $W = e^\Gamma$ is set. This results in a simple and nonanalytic form of the moment exponent, $K(q) = (C_1/(\alpha - 1))(q^\alpha - q)$. The universal multifractal model is the most promising model. It can be used to model the variability in several phenomena including turbulence, other geophysical phenomena, and several fractal-like appearances in natural objects and even man-made objects.

Based on this theory, we reconsider one of the basic questions in the observational study of ocean turbulence: how can one estimate energy intensity, or the energy input rate, from the vertical profile data of the energy dissipation rate, which has been commonly equated with the arithmetic mean over the profile. Our question pertains to whether one can obtain information regarding energy intensity beyond the arithmetic average. The answer is yes because we can construct a model for the turbulent cascade process and solve the inversion problem to obtain the energy input rate under an observational constraint. In this study, we first show that the observed profiles of the depth-averaged energy dissipation rate, ε_r , have a scaling property that is consistent with the universal multifractal model. Then, we construct a multiplicative cascade simulation model that describes the statistics in observational data. We propose a method to explain certain statistics of the observed profiles based on a simulation model and develop an inversion method to estimate the energy input rate. This result illustrates a systematic method of gaining further quantitative information from profile data.

Results

Analysis of observational data

Suppose we have the observational data of the energy dissipation rate, $\varepsilon_{r_0}(\vec{x})$, in bin width r_0 at horizontal position \vec{x} and their spatial average $\varepsilon_r(\vec{x})$ in width r . In terms of the universal multifractal model (14), the scaling of the statistical moments in the data takes the form

$$\frac{\langle (\varepsilon_{r_0}(\vec{x}))^q \rangle}{\langle (\varepsilon_r(\vec{x}))^q \rangle} = \left(\frac{r}{r_0} \right)^{K(q)}, \quad (4)$$

where $\langle \cdot \rangle$ denotes expectation. This implies that the expectation of the q -th moment at a scale over the one at another scale should be equal to the $K(q)$ -th power of the resolution ratio, regardless of the horizontal position \vec{x} . Based on Eq. (4), we perform a scaling analysis of observational data with respect to various moment exponents, q , by estimating the slope of the approximation straight line for the observational plots at various resolutions, r/r_0 ,

$$\left(\log r - \log r_0, \log \left(K^{-1} \sum_{k=1}^K (\varepsilon_{r_0}^{(k)})^q \right) - \log \left(K^{-1} \sum_{k=1}^K (\varepsilon_r^{(k)})^q \right) \right), \quad (5)$$

where the superscript (k) numbers the samples, which are also taken across all profiles.

The scalings for several moments are shown in Fig. 1. Gathering various slope values, the observational curve of $(q, K(q))$ in the range of $0 \leq q \leq 2$ is indicated in Fig. 2 in cyan. Considering the error for $K(q)$ at each q , the theoretical curve for the multifractal model (15) is fitted to the data. The best fit curve (black curve in Fig. 2) has a multifractal index of $\alpha = 1.74 \pm 0.01$, and the codimension of the mean is $C_1 = 0.393 \pm 0.001$. These values are largely consistent with previous results for atmospheric dissipation fields ($\alpha = 1.35 \pm 0.07$, $C_1 = 0.3 \pm 0.05$ for the horizontal shear of a velocity field²¹; $\alpha = 1.85 \pm 0.05$, $C_1 = 0.59 \pm 0.05$ for vertical kinetic energy flux²²).

Figure 3 shows the theoretical curve of extremes for the multifractal model (16) in black and the observational curve,

$$c_{\text{obs}}(\gamma) = -\log_\lambda [g(\gamma) Pr(\varepsilon_{r_0}/\varepsilon_L > \lambda^\gamma)], \quad \lambda = L/r_0, \quad (6)$$

in cyan, where $\lambda = 2^8$ is used, which is a typical scale ratio in the data. Note that the correction term,

$$g(\gamma) = \sqrt{2\pi\alpha c(\gamma) \log \lambda}, \quad (7)$$

serves to compensate for the prefactor in the asymptotic complementary cumulative distribution function, $g(\gamma)^{-1} e^{-c(\gamma)}$ [23, Eq. 1.2.11]. The two curves (16) and (6) appear to be in good agreement. Moreover, as our data have sampling dimension $D_s = \log_\lambda N_s \simeq \log 409 / \log(2^8) = 1.08$, the upper bound for q is calculated to be $q_s = 2.60$ (the slope of the navy blue line in Fig. 3), which justifies the range we set ($0 \leq q \leq 2$).

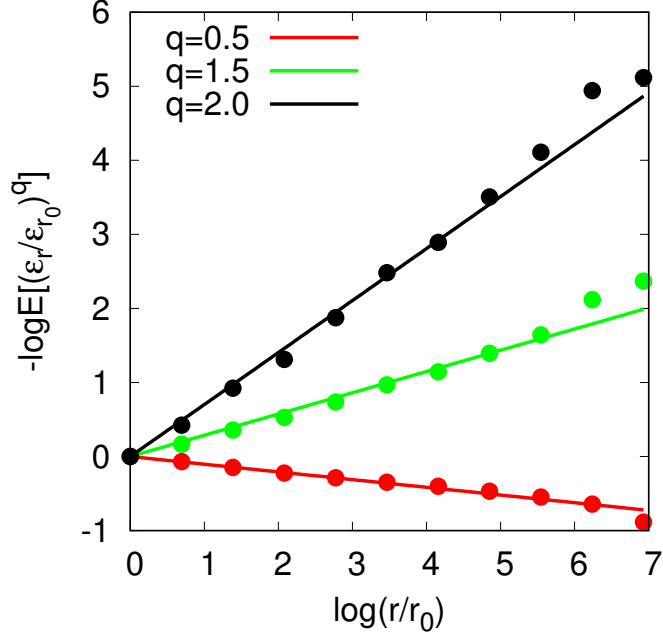


Figure 1. Scale dependency of the moments, $(\log(r/r_0), -\log \langle (\varepsilon_r/\varepsilon_{r_0})^q \rangle)$, where r_0 is the width of the observational bin. The moment scaling exponents are derived as $K(0.5) = -0.104 \pm 0.006$, $K(1.5) = 0.287 \pm 0.023$, $K(2.0) = 0.702 \pm 0.036$.

To demonstrate the appropriateness of the universal multifractal model, the histogram for the logarithm of bin values in observational data is shown in Fig. 4 and compared with samples from multiplicative cascade models, which are detailed in Methods. Each bin value, ε_{r_0} , is normalised by the arithmetic mean, ε_L , along the profile it belongs to. The histogram for the logarithm of bin data, $\log_{10}(\varepsilon_{r_0}/\varepsilon_L)$, appears to be in good agreement with the histogram of samples generated by the 8-step cascade model with stable Lévy generators (black; $\alpha = 1.74$, $C_1 = 0.393$) and in poor agreement with the histogram generated by the multifractal model with Gaussian generators (red; $\alpha = 2$, $C_1 = 0.397$).

Moreover, in the same manner as the correlation in Yaglom’s cascade, it is shown that the observational profiles have a power-law autocorrelation,

$$\langle \varepsilon(z)\varepsilon(z+\ell) \rangle \propto \ell^{-K(2)} = \ell^{-0.702}, \quad (8)$$

where z is depth. This also explains the discontinuous characteristics observed in the profiles (see Fig. 2(a)).

Simulation of cascade model

To estimate the energy input rate $\bar{\varepsilon}$ that corresponds to each observational profile, we firstly performed a Monte Carlo experiment with simulations of 1.024×10^{10} particles using the 8-step cascade model. The notation for the estimation study is summarised in Table 1, and constants and parameters are summarised in Table 2.

For each particle (or profile), we generate random numbers $\{\gamma_j | j = 1, 2, \dots, 256\}$ from $\bar{\varepsilon} = 1$ according to the procedure given in Methods, and add up the histograms for all the particles into the joint probability distribution $q_3(\bar{\gamma} - \hat{\gamma}, \hat{\gamma} - \tilde{\gamma}, \hat{\gamma} - \gamma^\sharp)$ (Fig. 5). Examples for conditional probability distribution $q_3(\bar{\gamma} - \hat{\gamma} | \hat{\gamma} - \tilde{\gamma}, \hat{\gamma} - \gamma^\sharp)$ are shown in Fig. 6. The conditional expectation for $\bar{\varepsilon}$ is not necessarily defined as a finite value because the posterior distribution of $\bar{\gamma}$ is neither Gaussian nor left-skewed stable. On the other hand, because the median and the percentiles, and thus the 95% confidence interval, for the distribution are always defined, we use them as the indices for estimation.

Identical twin experiment

Secondly, we estimated the posterior probability distribution for the energy input rate, $\bar{\varepsilon}$, by inverting the probability distribution that was computed from the simulation of the cascade model. Before applying it to real data, we performed an identical twin experiment using pseudo-observational data, whose energy input rates are given by hand, and thus the estimation result can be checked against them.

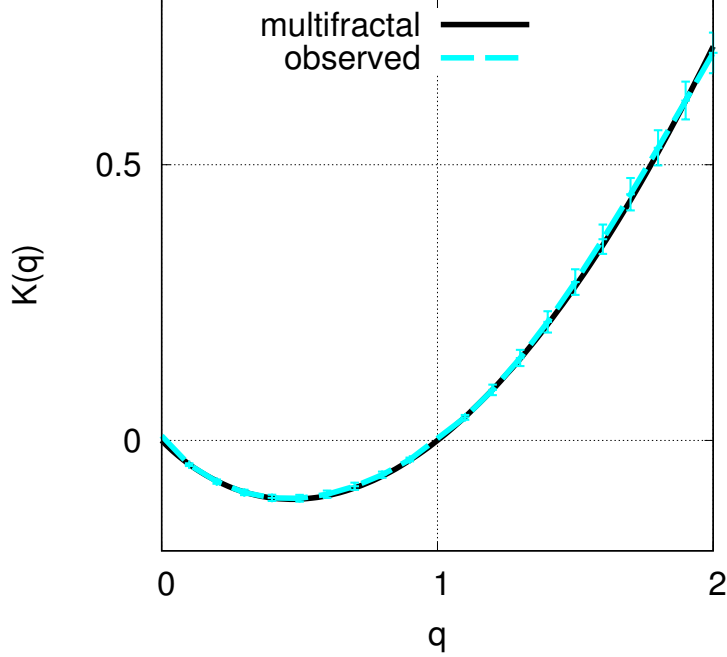


Figure 2. Moment scaling exponent $K(q)$ for observational data (cyan), and the best-fitting multifractal model (black). Each error bar in cyan shows the standard deviation for each $K(q)$.

The result of the identical twin experiment using $q_3(\bar{\gamma} - \hat{\gamma}|\hat{\gamma} - \tilde{\gamma}, \hat{\gamma} - \gamma^\sharp)$ is shown in Fig. 7a. In 28523 trials out of 30000 (about 95%), the true value of $\bar{\gamma}$ lies within the confidence interval, which ensures the validity of the estimation method. We also performed a reference experiment using $q_1(\bar{\gamma} - \hat{\gamma})$ (Fig. 7b), where the confidence interval and median show a common positional relation to the arithmetic mean. Comparing the case with q_3 to the one with q_1 , the root mean squares of the confidence intervals are 3.4 and 3.6 respectively, and 84% of trials in the former have narrower confidence intervals. This indicates the superiority of using information from $\tilde{\gamma}$ and γ^\sharp .

Real data experiment

By applying the same procedure to the real observational profiles of energy dissipation rate, each of which is represented by $\hat{\gamma}$, $\hat{\gamma} - \tilde{\gamma}$, and $\hat{\gamma} - \gamma^\sharp$, we derived the confidence interval of $\bar{\gamma}$ for the profile at each horizontal location. Estimated confidence intervals for real data are shown in Fig. 8b. Figure 9 shows the estimate for confidence intervals on the sections along 47°N and 137°E. Along 47°N, the median of $\bar{\epsilon}$ rarely exceeds $10^{-9} \text{m}^2 \text{s}^{-3}$, except around 172°E, 180°E, or 50°W. The peak of the arithmetic mean at 170°E is approximately 4 times larger than the median estimate, which could lead us to an overestimation.

Along 137°E, the median shows several significant peaks over $10^{-8} \text{m}^2 \text{s}^{-3}$ at around 2°N, 16°N, and 27 to 30°N. We could have underestimated the peaks at around 2°N and 27 to 30°N, but overestimated the one at around 16°N, if we only used the arithmetic mean.

For the analysis of observations on the section along 165°E, we should take care of the effect of repeated observation. In fact, the observations were performed twice at some horizontal locations there. For such cases, we simply assume that two independent realizations of a common $\bar{\gamma}$ are observed. In this regard, the inversion formula in Eq. (22) is modified as follows:

$$P(\bar{\gamma}|\hat{\gamma}_1, \hat{\gamma}_2) = \frac{P(\hat{\gamma}_1, \hat{\gamma}_2|\bar{\gamma})P(\bar{\gamma})}{\int P(\hat{\gamma}_1, \hat{\gamma}_2|\bar{\gamma})P(\bar{\gamma})d\bar{\gamma}} = \frac{P(\hat{\gamma}_1|\bar{\gamma})P(\hat{\gamma}_2|\bar{\gamma})P(\bar{\gamma})}{\int P(\hat{\gamma}_1|\bar{\gamma})P(\hat{\gamma}_2|\bar{\gamma})P(\bar{\gamma})d\bar{\gamma}} = \frac{q_1(\bar{\gamma} - \hat{\gamma}_1)q_1(\bar{\gamma} - \hat{\gamma}_2)}{\int q_1(\bar{\gamma} - \hat{\gamma}_1)q_1(\bar{\gamma} - \hat{\gamma}_2)d\bar{\gamma}}, \quad (9)$$

where two observations are distinguished by subscript 1, 2. This distribution is nothing but the normalised product of the two distributions. When considering $\tilde{\gamma}$ and γ^\sharp , the same procedure as in Eq. (9) applies to the conditional distribution:

$$\begin{aligned} P(\bar{\gamma}|\hat{\gamma}_1, \hat{\gamma}_2, \hat{\gamma}_1 - \tilde{\gamma}_1 = u_1, \hat{\gamma}_1 - \gamma_1^\sharp = v_1, \hat{\gamma}_2 - \tilde{\gamma}_2 = u_2, \hat{\gamma}_2 - \gamma_2^\sharp = v_2) \\ = \frac{q_3(\bar{\gamma} - \hat{\gamma}_1|u_1, v_1)q_3(\bar{\gamma} - \hat{\gamma}_2|u_2, v_2)}{\int q_3(\bar{\gamma} - \hat{\gamma}_1|u_1, v_1)q_3(\bar{\gamma} - \hat{\gamma}_2|u_2, v_2)d\bar{\gamma}}. \end{aligned} \quad (10)$$

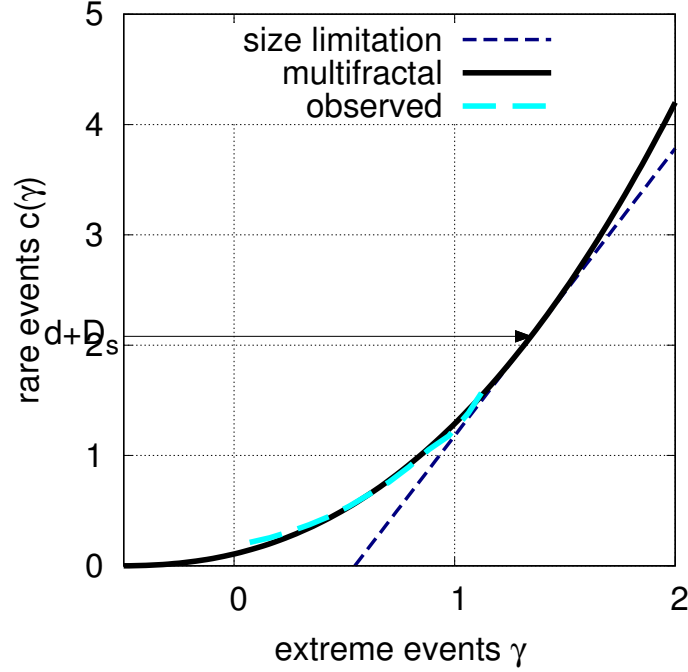


Figure 3. Codimension $c(\gamma)$ of singularities γ for multifractal model (black). The corresponding curve for observation is shown for reference (cyan). Sampling dimension D_s and the limitation for the moment exponent (the slope of the navy blue line) are also shown.

Figure 10b shows the estimation of confidence interval along 165°E , by taking into account the effect of repeated observation. For comparison, the result without considering the repeated observation is shown in Fig. 10a, where we assume that each observation is for different $\bar{\gamma}$. We can see that the confidence intervals become narrower when considering the effect of repeated observation. Furthermore, along 165°E , the median shows a broad and significant peak over $10^{-8}\text{m}^2\text{s}^{-3}$ at around 30°N .

Discussion

We have analysed the observed data obtained from oceanic turbulence and shown that the vertical sequences of energy dissipation rates have an intermittent structure that obeys a scaling law. Furthermore, we have proposed a method of estimating the energy input rate given observations by utilising that property.

1. For scaling in the observed profiles, the statistical property of our data is consistent with the universal multifractal model, which has a moment scaling exponent of $K(q) = (C_1/(\alpha - 1))(q^\alpha - q)$ with a multifractal index $\alpha = 1.74$ and the codimension of the mean $C_1 = 0.393$. This result elucidates the universality inherent in the oceanic turbulence data.
2. The energy input rate and its uncertainty can be estimated by an inference using the result of Monte Carlo simulation of the cascade model. This method utilises the observed values of arithmetic mean, geometric mean, and quadratic mean over a profile. The estimate provides additional information about the uncertainty of the energy input rate, which is more accurate than the one obtained solely from the arithmetic mean.
3. Theoretically, this technique can easily be extended by utilising more statistics over a profile than the arithmetic mean, geometric mean, and quadratic mean. Note however that such extension may easily provoke the curse of dimensionality, and thus can become impractical.
4. Thus, we have found an answer to the question: ‘How can one estimate energy input rate from the vertical profile data of the energy dissipation rate?’ By analysing the intermittency in the observed data, we can construct a multiplicative cascade model based on the universal multifractal formalism, which can reproduce the statistics of the data. Then, the energy input rate given observed data is estimated by inverting the probability distribution obtained from Monte Carlo simulations of the cascade model.

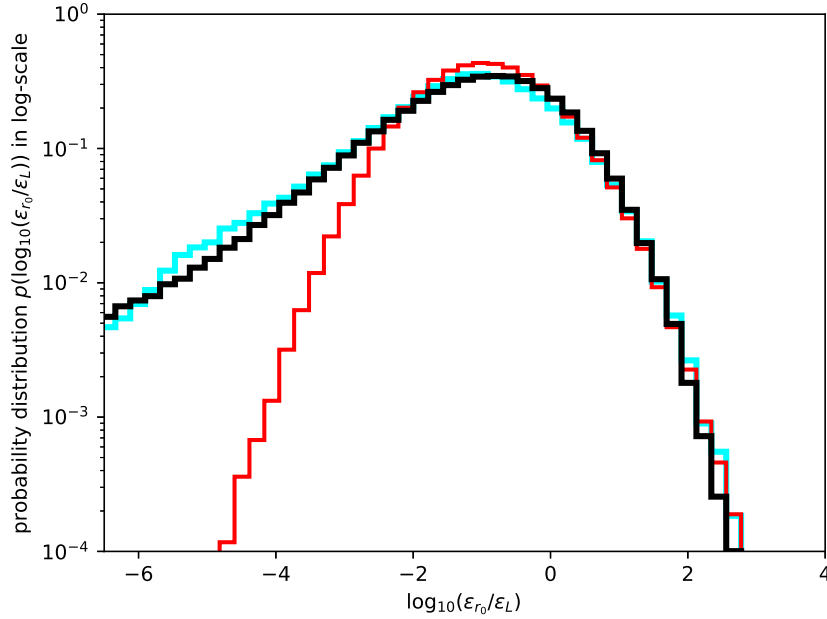


Figure 4. Distribution of the logarithm of observational data normalised for each profile (cyan) and comparison with the statistics of samples generated from multiplicative cascade with Gaussian/stable Lévy generators (red/black).

5. Even though we have used a discrete cascade model for simplicity and computational viability, we can extend it to a continuous cascade²⁴, which may improve the estimation accuracy at the cost of computational burden.

Methods

Observational data

In this section, we describe the turbulence observational data employed in this study. The turbulence observational data were retrieved from the Pacific ocean (Fig. 12)²⁵, and they comprise 409 profiles, each of which typically extends over a depth of 2000 to 6000 m below the sea surface, with observational points every 5 to 10 m.

The turbulent energy dissipation rates, ε_{r_0} , where r_0 is the bin width, were estimated as follows: Microscale temperature fields were observed using the fast-response Fasttip Probe model 07 (FP07) thermistors attached to frames for measuring conductivity, temperature, and depth (CTD) as common oceanographic observational platforms. ε_{r_0} was derived by detecting the Batchelor wavenumber²⁶ and fitting²⁷ a theoretical spectrum²⁸ to the observed temperature vertical gradient spectra after correcting the spectra with a double-pole function with a time constant of 3ms²⁹. Each data point was evaluated for a depth interval of approximately 10m with half overlap to yield 5dbar interval data. Herein, we included all data without any quality screening to consider the extreme values, which are important for investigating intermittency.

We estimated the turbulent energy dissipation rate from temperature measurement in each observational bin with a width of $r_0 \simeq 10\text{m}$ by utilising a fitting method based on analytical spectral closure.

Turbulent energy dissipation rate ε_{r_0} is estimated from the spectra of the temperature vertical gradient $\partial T'/\partial z$ using fast-response thermistor FP07 measurements, with a time constant of approximately $7 \times 10^{-3}\text{s}$ (Fig. 11). The Fourier-transformed observed wavenumber temperature gradient spectrum (blue curve) is numerically integrated between the lowest wavenumber and the highest wavenumber at which the spectrum amplitude is more than 1.5 times the noise spectrum (light-blue curve), which is inherent in the instrument, and thermal dissipation rate χ is obtained ($= 6\kappa_T \left(\frac{\partial T'}{\partial z}\right)^2$, where κ_T is the molecular thermal diffusivity). ε_{r_0} is estimated by detecting wavenumber k_P at the peak of the temperature gradient spectrum to yield the Batchelor wavenumber, $k_B (= \left(\frac{\varepsilon_{r_0}}{\nu\kappa_T}\right)^{\frac{1}{4}}/2\pi)$ ²⁶, as $k_B = \sqrt{6q_K}k_P$, at which molecular thermal diffusion begins to work. This peak is detected by fitting the theoretically derived universal temperature gradient spectrum²⁸, $S_{\text{theoretical}}$ (red curve) with the form given in Roget et al. (2006)³⁰, to the observed spectrum using the maximum likelihood method developed by Ruddick

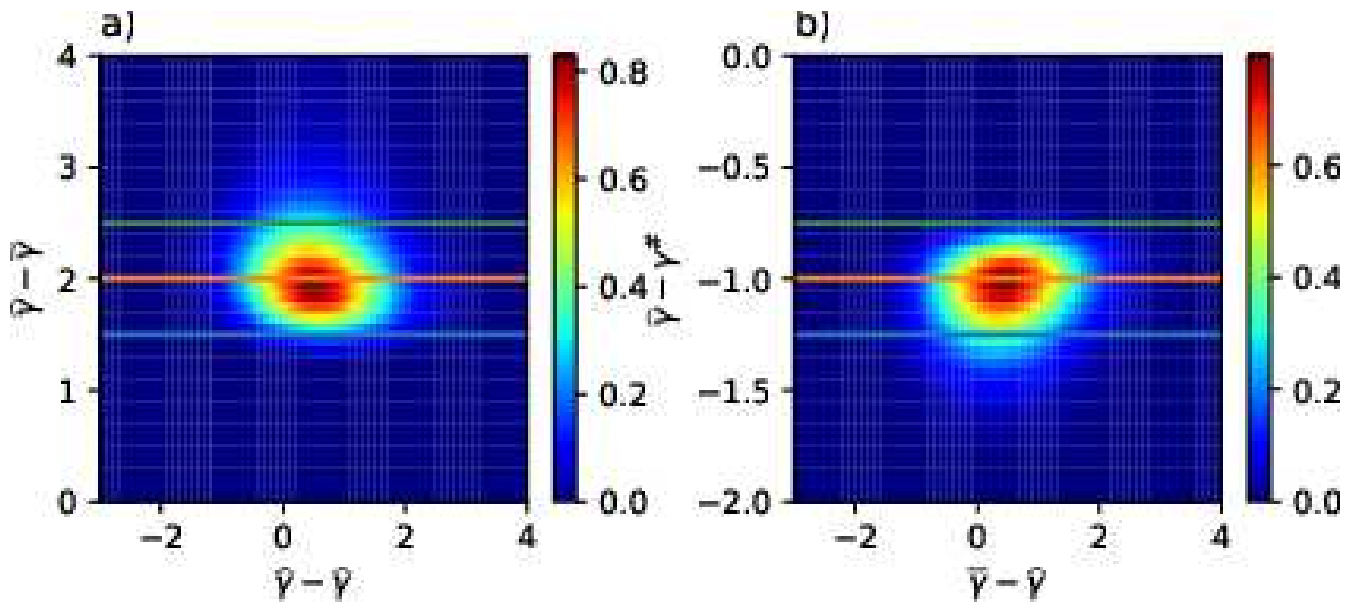


Figure 5. Examples of cross section cut of joint probability distribution $q_3(\bar{\gamma} - \hat{\gamma}, \hat{\gamma} - \tilde{\gamma}, \hat{\gamma} - \gamma^\#)$. a) section cut $q_3(\bar{\gamma} - \hat{\gamma}, u, -1)$ with section lines $u = 1.5, 2, 2.5$, and b) section cut $q_3(\bar{\gamma} - \hat{\gamma}, 2, v)$ with section lines $v = -1.25, -1, -0.75$.

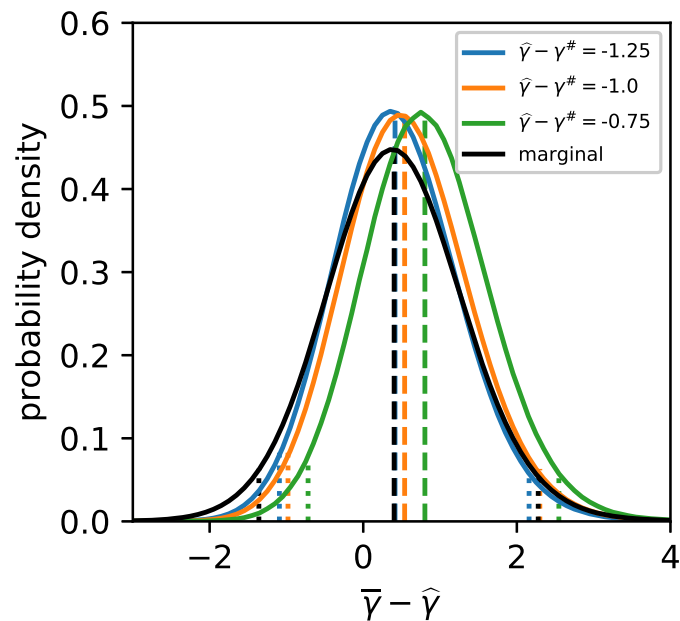


Figure 6. Examples of conditional probability distribution $q_3(\cdot|u, v)$ (coloured) and marginal probability distribution $q_1(\cdot)$ (black), along with median (broken lines) and 95% confidence intervals (dotted lines). Conditional probabilities are for $u = 2; v = -1.25, -1, -0.75$.

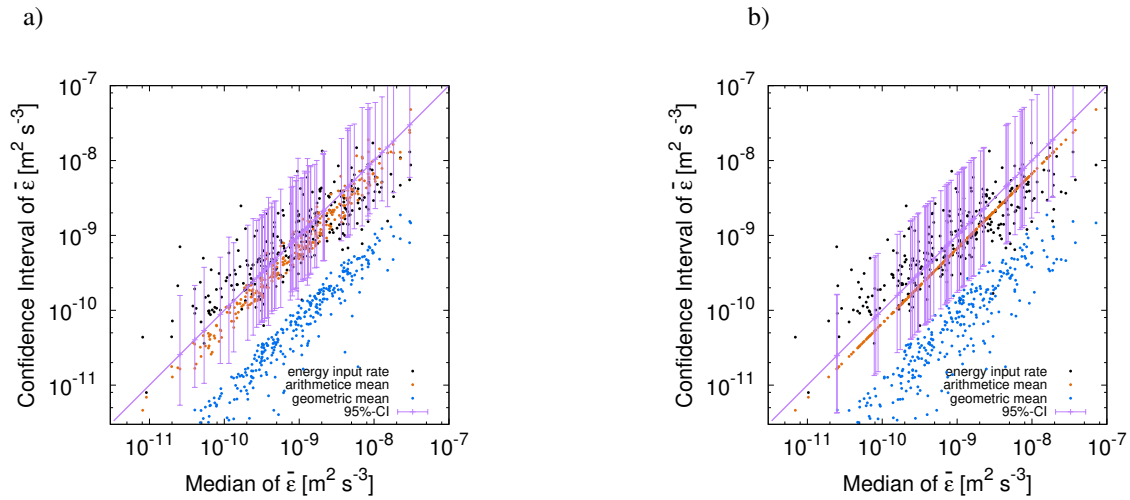


Figure 7. Result of identical twin experiments. Median (horizontal axis) versus confidence interval (vertical axis). a) result using conditional probability distribution $q_3(\cdot|u, v)$, and b) result using marginal probability distribution $q_1(\cdot)$. For given values of the median on the horizontal axis, the points on the vertical axis indicate the values of the confidence interval (purple), arithmetic mean (orange), geometric mean (blue), and the energy input rate (black). For readability, 300 points and 60 intervals are drawn out of 30000 trials.

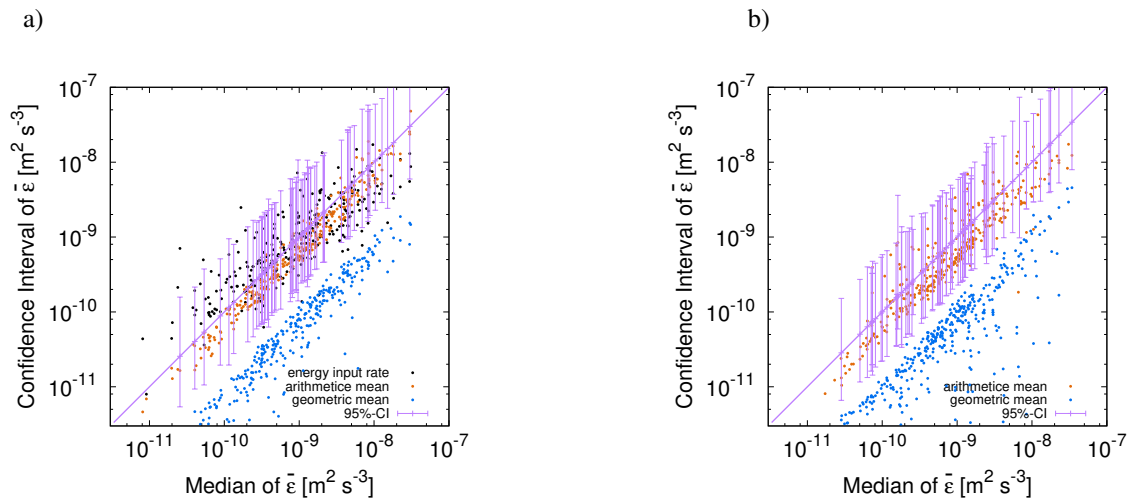


Figure 8. Result of real data experiment in comparison with that of identical twin experiment. Median (horizontal axis) versus confidence interval (vertical axis). a) result of identical twin experiment, and b) result of real data experiment. For given values of the median on the horizontal axis, the points on the vertical axis indicate the values of the confidence interval (purple), arithmetic mean (orange), geometric mean (blue), and the energy input rate (black). In b, only 70 confidence intervals out of 353 trials are drawn for readability.

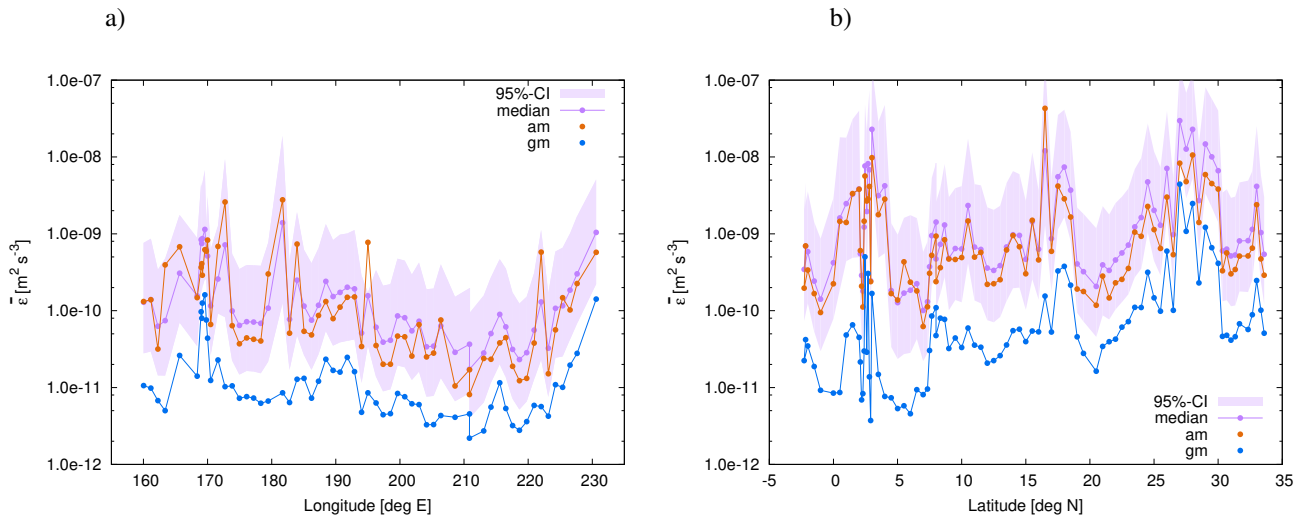


Figure 9. Geographical distribution of confidence intervals. 47°N (a) and 137°E (b). Horizontal axis shows the location, and the values of median (purple dots) and confidence interval (purple shade), arithmetic mean (orange), and geometric mean (blue) are on the vertical axis.

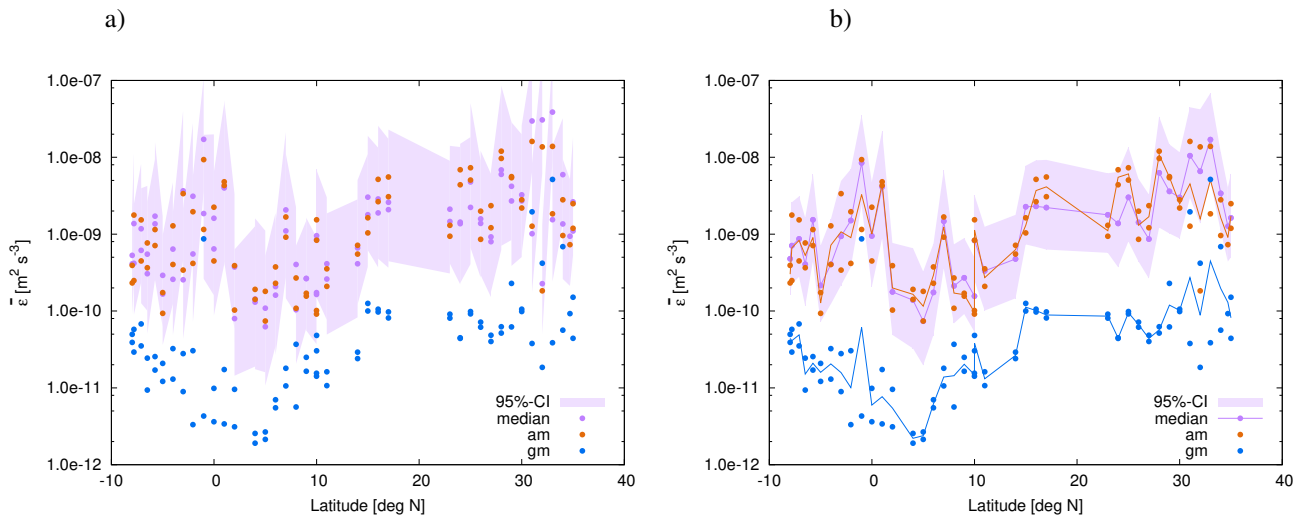


Figure 10. Geographical distribution of confidence intervals. 165°E. The effect of repeated observation is considered in a), but not in b). Horizontal axis shows the location, and the values of median (purple dots) and confidence interval (purple shade), arithmetic mean (orange), and geometric mean (blue) are on the vertical axis.

et al.²⁷ with the parameters proposed by Peterson and Fer³¹.

$$S_{\text{theoretical}}(k; k_B) = \frac{\chi \sqrt{q_K}}{\kappa_T k_B} y_k^2 \frac{\exp(-\sqrt{6} y_k)}{y_k},$$

where $y_k = \sqrt{q_K} k / k_B$ and q_K is the Kraichnan constant. q_K has been estimated as $q_K = 3.4 - 7.9$ (3.41: Antonia and Orlandi³²; 5.26 ± 0.25 : Bogucki et al.^{33,34}, 7.9 ± 2.5 : Sanchez et al.³⁵). We use a fixed value of $q_K = 5.26$, which was introduced in Bogucki et al.^{33,34}. The Kraichnan spectrum is the modified version of the Batchelor spectrum²⁶ considering the intermittency of strain fields. See Goto et al.(2016, 2018)^{25,29} for other detailed estimation procedures.

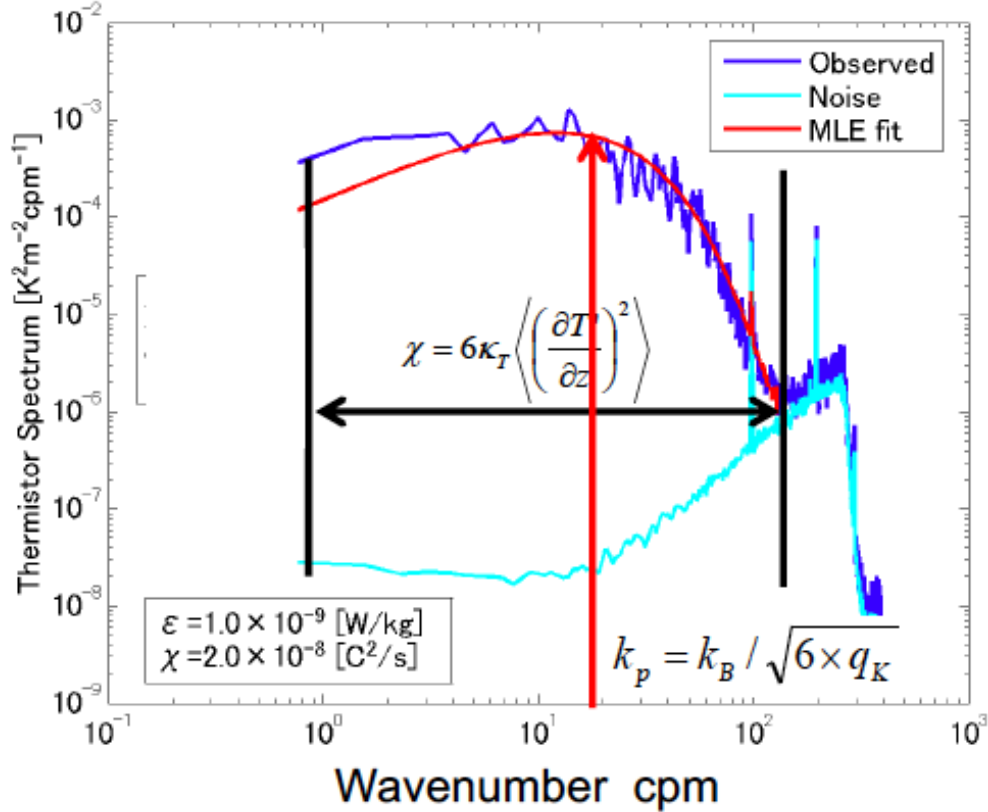


Figure 11. Example of observational wavenumber temperature gradient spectrum (blue curve), noise spectrum (light blue), and fitted theoretical spectrum (red) to detect the wavenumber at spectrum peak k_p to yield Batchelor wavenumber k_B given ϵ_{r_0} .

Given that the observation is performed at resolution r_0 , we restrict our investigation to the intermittency occurring at larger scales, $r > r_0$. Let r_0 be the bin width, \vec{x}_j the horizontal coordinate of the j -th profile, and z_k the vertical coordinate of the k -th point in the j -th profile. These positive-valued data have the following characteristics:

1. Each profile defines an ordered set,

$$\left\{ \epsilon_{r_0}(\vec{x}_j, z_{k_j}) \mid k_j = 1, 2, \dots, K_j \right\}, \quad (11)$$

which exhibits an extremely erratic evolution that impedes the recognition of a continuous curve along the depth direction (Fig. 13(a)).

2. After taking the logarithm of the values, the sequences appear to be more continuous (Fig. 13(b)).
3. If we normalise each value with the arithmetic mean along the profile it belongs to, the histogram of the logarithmic

values,

$$\left\{ \log \left(\frac{\varepsilon_{r_0}(\vec{x}_j, z_{k_j})}{\varepsilon_L(\vec{x}_j)} \right) \middle| j = 1, 2, \dots, J; k_j = 1, 2, \dots, K_j \right\}, \quad \varepsilon_L(\vec{x}_j) \stackrel{\text{def}}{=} K_j^{-1} \sum_{k_j} \varepsilon_{r_0}(\vec{x}_j, z_{k_j}) \quad (12)$$

appears as an asymmetric distribution (cyan in Fig. 4), which is discussed below.

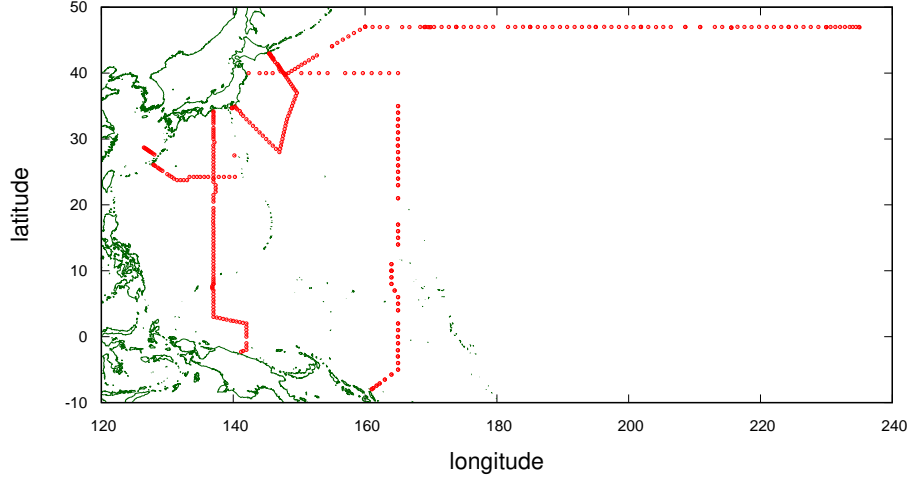


Figure 12. Horizontal locations of the observed profiles (red) and land–sea boundaries (green). The units of longitude and latitude are °E and °N, respectively.

Multifractal analysis

We perform the scaling analysis of the moments to derive the moment scaling exponent within the universal multifractal framework. Although the analysis could be extended to multidimensional objects³⁶, the limited number of samples (409 profiles) prevents us from a meaningful treatment in a multidimensional framework. Therefore, we treat each profile as an independent sample, and analyse the statistical structure of the 1-dimensional object. One exception applies for repeated observations at the same horizontal location (see Results).

Universal multifractal model

The basic formulation of the universal multifractal model is as follows^{36,37}: Suppose we have a multifractal field, ε_λ , at resolution λ ($= L/r$), where r is the observational scale and L is the outer scale. The field is normalised by the mean, $\langle \varepsilon_\lambda \rangle = \langle \varepsilon \rangle$, which is conserved at all scales.

The probability of exceeding a scale-dependent threshold, λ^γ , varies according to singularity γ as

$$Pr(\varepsilon_\lambda \geq \lambda^\gamma) \approx \lambda^{-c(\gamma)}, \quad (13)$$

where $c(\gamma)$ is the codimension function and \approx represents the equality up to the multiplication of a slowly varying function of γ . Thus, the multifractal model is characterised by the property that the codimension varies with the singularity. This relation is equivalently represented as the scaling of the statistical moment of any order, q ,

$$\langle (\varepsilon_\lambda)^q \rangle = \lambda^{K(q)}, \quad (14)$$

where $K(q)$ is the moment scaling function. The two functions, $K(q)$ and $c(\gamma)$, are actually compatible by the Legendre transformation because the moment generation function can be written in terms of the occurrence probability of singular

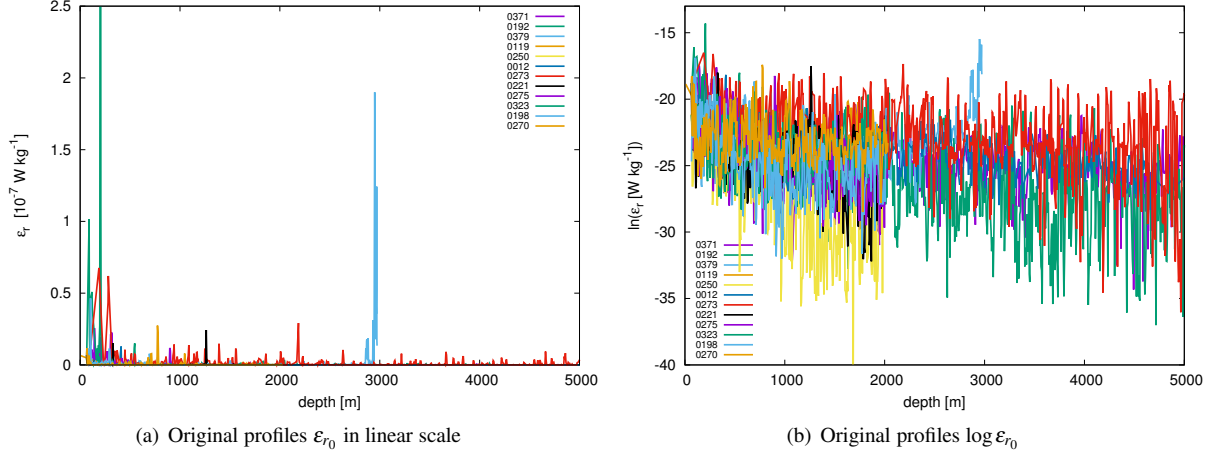


Figure 13. Appearances of observed profiles.

events using the saddle-point approximation, $\langle (\varepsilon_\lambda)^q \rangle = \int \lambda^{q\gamma} dp(\gamma) \approx \lambda^{\max_\gamma \{q\gamma - c(\gamma)\}}$ ³⁸. Functions $K(q)$ and $c(\gamma)$ determine the variability of multifractal field ε_λ across the scales, λ .

Owing to a generalisation of the central limit theorem, many multiplicative processes composed of different generators converge to a universal multifractal^{18,39}, whose moment exponent has the following form:

$$K(q) = \frac{C_1}{\alpha - 1} (q^\alpha - q), \quad (15)$$

where $0 \leq \alpha \leq 2$ is the multifractal index and C_1 is the codimension of the mean. This also satisfies probability normalisation, $K(0) = 0$, and energy conservation, $K(1) = 1$. The Legendre transformation of this gives $c(\gamma)$ in the following form:

$$c(\gamma) = C_1 \left(\frac{\gamma}{C_1 \alpha'} + \frac{1}{\alpha} \right)^{\alpha'}, \quad (16)$$

where $1/\alpha + 1/\alpha' = 1$.

Estimations based on the cascade model

In this section, we discuss how to estimate the energy input rate, $\bar{\varepsilon}$, by utilising the information obtained from an observational profile. Even though it is primarily indicated by the arithmetic average of vertical data values, as shown in the previous subsection, there still is a requirement for obtaining uncertainty information. For this purpose, we will estimate the confidence interval, the interval within which ‘the population mean’, $\bar{\gamma}$, is expected to lie with a defined probability. Although the arithmetic mean over a profile is the primary measure for the sample, the characteristics of the population can also be evaluated by using the joint probability density of several different sample statistics, obtained from Monte Carlo simulation of the cascade model. The notation used in this section is summarised in Table 1, and constants and parameters are summarised in Table 2.

Multiplicative cascade simulation

To examine the relationship between various statistical quantities derived from observational profiles, we construct a simulation model for the multiplicative cascade by following the procedure described in Schmitt (2003)⁴⁰, as shown in Fig. 14. Each building block, Γ_{ik} , is a generator that obeys a left-skewed stable distribution, $S_\alpha(\sigma h^{1/\alpha}, -1, -\widehat{\sigma}_\alpha^\alpha h)$, with $h = \log 2$, $\widehat{\sigma}_\alpha^\alpha \stackrel{\text{def}}{=} \sigma^\alpha / \cos(\frac{\pi}{2}(2 - \alpha)) = C_1 / (\alpha - 1)$ ²³.

Consider a fixed horizontal position \vec{x} . Let $\bar{\varepsilon} = \exp(\bar{\gamma})$ be the energy input rate from an external force at \vec{x} , the number of steps be $n = \log_2 \frac{L}{r}$, $0 \leq i \leq n$ be scale index, and $1 \leq j \leq 2^n$ be spatial index. The cascade simulation is performed for variable $X_{i,j}$ as follows.

1. For each spatial index $j = 1, 2, \dots, 2^n$, set $X_{0,j} = \bar{\gamma}$.
2. For each scale index $i = 1, \dots, n$, repeat the following steps:

Table 1. Notation for the estimation study

Name	Notation	Definition
Index for vertical position	j	$1, 2, 3, \dots, 2^n$
Energy dissipation rate	ε_j	
Logarithm of energy dissipation rate	γ_j	$\log \varepsilon_j$
Energy input rate	$\bar{\varepsilon}$	
Logarithm of energy input rate	$\bar{\gamma}$	$\log \bar{\varepsilon}$
Stable Lévy generators	Γ_{ik}	$\sim S_\alpha(\sigma h^{1/\alpha}, -1, -\widehat{\sigma}_\alpha^\alpha h)$
Width of Lévy generator	-	$\sigma h^{1/\alpha}$
Shift of Lévy generator	-	$-\widehat{\sigma}_\alpha^\alpha h = -\frac{\sigma^\alpha}{\cos(\frac{\pi}{2}(2-\alpha))} h = -\frac{C_1}{\alpha-1} h$
Logarithm of arithmetic mean	$\widehat{\gamma}$	$\log \left(2^{-n} \sum_{j=1}^{2^n} e^{\gamma_j} \right)$
Logarithm of geometric mean	$\widetilde{\gamma}$	$2^{-n} \sum_{j=1}^{2^n} \gamma_j$
Logarithm of quadratic mean	$\gamma^\#$	$2^{-1} \log \left(2^{-n} \sum_{j=1}^{2^n} e^{2\gamma_j} \right)$
Marginal probability distribution	q_1	Probability distribution of $\bar{\gamma} - \widehat{\gamma}$; $q_1(\cdot) = \int \int q_3(\cdot, u, v) du dv$
Joint probability distribution	q_3	Probability distribution of $(\bar{\gamma} - \widehat{\gamma}, \widehat{\gamma} - \widetilde{\gamma}, \widetilde{\gamma} - \gamma^\#)$

Table 2. Constants and Parameters for the estimation study

Meaning	Parameter	Value
Number of steps in cascade	n	8
Number of vertical points	2^n	256
Step size of cascade	h	$\log 2$
Number of samples in Monte Carlo simulation	M	1.024×10^{10}
Multifractal index	α	1.74
Codimension of the mean	C_1	0.393
Width of bins in histogram of q_3	(w_1, w_2, w_3)	(0.1, 0.1, 0.05)
Number of bins in histogram of q_3	(n_1, n_2, n_3)	(500, 200, 200)
Number of profiles in identical twin exp.	-	30000
Number of observed profiles (Obs.)	-	409
Obs. with more than 2^n vertical points	-	353

- For each spatial block $k = 1, 2, \dots, 2^i$, perform the following steps:
 - (a) Generate a random variable, ξ_{ik} , which obeys $S_\alpha(1, -1, 0)$ ⁴¹.
 - (b) For each spatial index $j = (k-1) \cdot 2^{n-i} + 1, \dots, k \cdot 2^{n-i}$, downscale X by

$$X_{i,j} = X_{i-1,j} + \Gamma_{i,k}, \quad \Gamma_{i,k} \stackrel{\text{def}}{=} -\widehat{\sigma}_\alpha^\alpha h + \sigma h^{\frac{1}{\alpha}} \xi_{ik}. \quad (17)$$

- For each spatial index $j = 1, 2, \dots, 2^n$, set $\gamma_j = X_{n,j}$.

The output, γ_j , represents the logarithm of the energy dissipation rate at the horizontal position, \vec{x} , and the vertical position, $z_j \in [(j-1)r_n, jr_n]$ at resolution $r_n = L/2^n$. By using the Gauss symbol, the cascade process can be more compactly represented as

$$\gamma_j = \bar{\gamma} + \sum_{i=1}^n \Gamma_{i, [(j-1)/2^{n-i}]+1}, \quad j = 1, 2, \dots, 2^n. \quad (18)$$

An important implication in this formulation is that the arithmetic average of the vertical data points is not necessarily equal to the energy input rate because the cascade process has a fluctuating nature. In other words, a realisation of the vertical average, $\varepsilon_L = 2^{-n} \sum_{j=1}^{2^n} \exp(\gamma_j)$, is not always equal to $\bar{\varepsilon}$, whereas expectation $\mathbb{E}[\varepsilon_L]$ is $\bar{\varepsilon}$. Below, we focus mainly on the relationship between the arithmetic average over a profile and the energy input rate. We perform statistical estimations from one to the other of these quantities based on the cascade model.

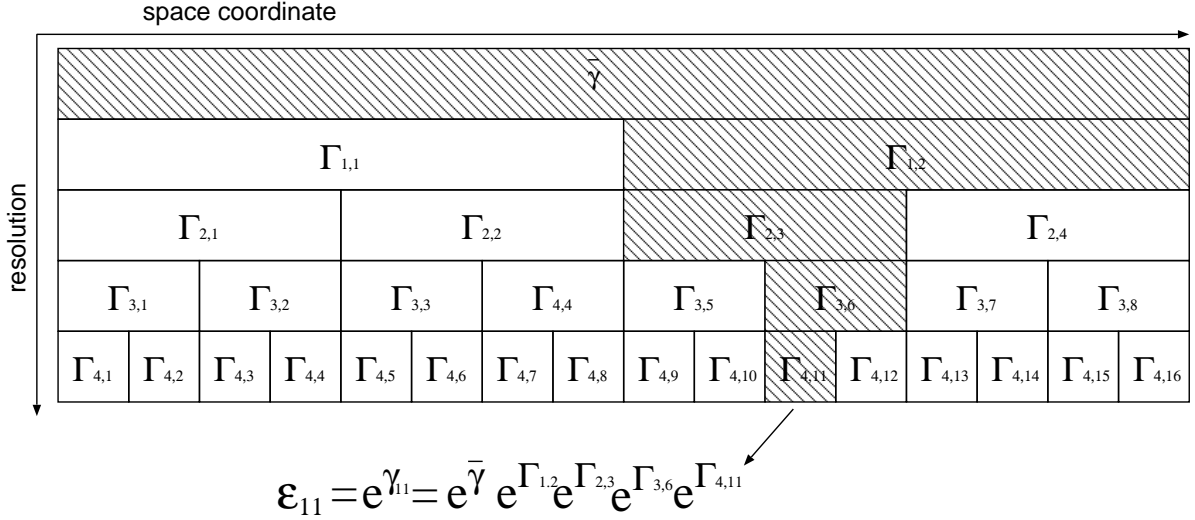


Figure 14. Schematic of the multiplicative cascade model. The energy dissipation rate at z_{11} at resolution $r_4 = L/2^4$ is considered as an example.

Estimation of the energy input rate

We assume that each set of γ_j 's is generated by an n -step cascade model as in Eq. (18). What we want to estimate here is the energy input rate $\bar{\gamma}$, which corresponds to a population mean, using the information from observed data $\{\gamma_j | j = 1, 2, \dots, 2^n\}$. In this regard, in addition to the arithmetic mean $\hat{\gamma}$, which corresponds to $K(1)$ in Fig 1, we can also use other moments over a profile, e.g., geometric mean $\tilde{\gamma}$ and quadratic mean γ^\sharp , which correspond to $K'(0)$ and $K(2)$, respectively. We take note of the following expressions based on Eq. (18):

$$\hat{\gamma} = \bar{\gamma} + \log \left\{ 2^{-n} \sum_{j=1}^{2^n} \exp \left(\sum_{i=1}^n \Gamma_{i, [(j-1)/2^{n-i} + 1]} \right) \right\}, \quad (19)$$

$$\tilde{\gamma} = \bar{\gamma} + 2^{-n} \sum_{j=1}^{2^n} \sum_{i=1}^n \Gamma_{i, [(j-1)/2^{n-i} + 1]}, \quad (20)$$

$$\gamma^\sharp = \bar{\gamma} + \frac{1}{2} \log \left\{ 2^{-n} \sum_{j=1}^{2^n} \exp \left(2 \sum_{i=1}^n \Gamma_{i, [(j-1)/2^{n-i} + 1]} \right) \right\}, \quad (21)$$

where we find the term $\bar{\gamma}$ is factored out. Therefore, $\bar{\gamma} - \hat{\gamma}$, $\hat{\gamma} - \tilde{\gamma}$, and $\hat{\gamma} - \gamma^\sharp$ are independent of $\bar{\gamma}$, and also dimensionless.

The structure of the cascade model implies that the appearance probability of $\hat{\gamma}$ given $\bar{\gamma}$ is determined only by their difference: $P(\hat{\gamma}|\bar{\gamma}) = q_1(\bar{\gamma} - \hat{\gamma})$. Furthermore, by assuming that we have no prior information about $\bar{\gamma}$, Bayes' theorem applies to invert it into the posterior probability for $\bar{\gamma}$, as follows.

$$P(\bar{\gamma}|\hat{\gamma}) = \frac{P(\hat{\gamma}|\bar{\gamma})P(\bar{\gamma})}{\int P(\hat{\gamma}|\bar{\gamma})P(\bar{\gamma})d\bar{\gamma}} = q_1(\bar{\gamma} - \hat{\gamma}). \quad (22)$$

The information on $\tilde{\gamma}$ and γ^\sharp is encoded in joint probability distribution $q_3(\bar{\gamma} - \hat{\gamma}, \hat{\gamma} - \tilde{\gamma}, \hat{\gamma} - \gamma^\sharp)$ computed from Monte Carlo simulation of the cascade model, and the conditional probability distribution is derived as

$$q_3(\bar{\gamma} - \hat{\gamma}, \hat{\gamma} - \tilde{\gamma}, \hat{\gamma} - \gamma^\sharp) = \frac{q_3(\bar{\gamma} - \hat{\gamma}, \hat{\gamma} - \tilde{\gamma}, \hat{\gamma} - \gamma^\sharp)}{\int q_3(\bar{\gamma} - \hat{\gamma}, \hat{\gamma} - \tilde{\gamma}, \hat{\gamma} - \gamma^\sharp) d\bar{\gamma}}. \quad (23)$$

The similar procedure as in Eq. (22) applies to obtain the posterior probability:

$$P(\bar{\gamma}|\hat{\gamma}, \hat{\gamma} - \tilde{\gamma} = u, \hat{\gamma} - \gamma^\sharp = v) = q_3(\bar{\gamma} - \hat{\gamma}|u, v), \quad (24)$$

under the constraint of $\hat{\gamma} - \tilde{\gamma} = u$, $\hat{\gamma} - \gamma^\sharp = v$.

On the basis of the above formulation, we performed an identical twin experiment using the following procedure.

1. Perform a Monte Carlo experiment to obtain $q_3(\bar{\gamma} - \hat{\gamma}, \hat{\gamma} - \tilde{\gamma}, \hat{\gamma} - \gamma^\#)$.
 - (a) Set the energy input rate to $\bar{\gamma} = 0$.
 - (b) Create many random samples of the profile using the cascade model according to the procedure in the previous section.
 - (c) Add up the frequency of occurrence to derive the joint probability distribution $q_3(\bar{\gamma} - \hat{\gamma}, \hat{\gamma} - \tilde{\gamma}, \hat{\gamma} - \gamma^\#)$.
2. Set the energy input rate $\bar{\gamma}$ to a random number.
3. Create a random sample of the profile using the cascade model according to the procedure in the previous section.
4. Calculate the parameters $\hat{\gamma}, \hat{\gamma} - \tilde{\gamma}, \hat{\gamma} - \gamma^\#$ for the profile.
5. Compute the conditional probability distribution $P(\bar{\gamma} | \hat{\gamma}, \hat{\gamma} - \tilde{\gamma}, \hat{\gamma} - \gamma^\#)$.
6. Calculate the median and 95% confidence interval for the estimated $\bar{\gamma}$.
7. Compare the estimate of $\bar{\gamma}$ with the true value of $\bar{\gamma}$.

The same procedure applies to real data experiment, except that $\bar{\gamma}$ in 2 is unknown, as follows.

1. Pick an observed profile, and calculate the parameters $\hat{\gamma}, \hat{\gamma} - \tilde{\gamma}, \hat{\gamma} - \gamma^\#$ for the profile.
2. Compute the conditional probability distribution $P(\bar{\gamma} | \hat{\gamma}, \hat{\gamma} - \tilde{\gamma}, \hat{\gamma} - \gamma^\#)$, using the joint probability distribution $q_3(\bar{\gamma} - \hat{\gamma}, \hat{\gamma} - \tilde{\gamma}, \hat{\gamma} - \gamma^\#)$ obtained from the Monte Carlo experiment.
3. Calculate the median and 95% confidence interval for the estimated $\bar{\gamma}$.

References

1. Gregg, M., Cox, C. & Hacker, P. Vertical Microstructure Measurements in the Central North Pacific. *J. Phys. Oceanogr.* **3**, 458–469 (1973).
2. Munk, W. & Wunsch, C. Abyssal recipes II: Energetics of tidal and wind mixing. *Deep. Sea Res. Part I: Oceanogr. Res. Pap.* **45**, 1977–2010 (1998).
3. Waterhouse, A. F. *et al.* Global patterns of diapycnal mixing from measurements of the turbulent dissipation rate. *J. Phys. Oceanogr.* **44**, 1854–1872, DOI: [10.1175/JPO-D-13-0104.1](https://doi.org/10.1175/JPO-D-13-0104.1) (2014). <https://doi.org/10.1175/JPO-D-13-0104.1>.
4. Waterhouse, A. & McKinnon, J. Datasets obtained from ocean microstructure profilers (2014).
5. Pope, S. B. *Turbulent flows* (Cambridge university press, 2000).
6. Richardson, L. F. *Weather Prediction by Numerical Process* (Cambridge University, Cambridge, 1922).
7. Kolmogorov, A. N. The local structure of turbulence in incompressible viscous fluid for very large Reynolds numbers. *Cr Acad. Sci. URSS* **30**, 301–305 (1941).
8. Landau, L. D. & Lifshitz, E. M. Fluid mechanics. *Fluid Mech. Second. Ed. 1987. Pergamon, Oxf.* (1987).
9. Kolmogorov, A. N. A refinement of previous hypotheses concerning the local structure of turbulence in a viscous incompressible fluid at high Reynolds number. *J. Fluid Mech.* **13**, 82–85 (1962).
10. Gurvich, A. & Zubkovskii, S. On experimental estimate of the fluctuations of turbulent energy dissipation. *Izv. Akad. Nauk SSSR, Ser. Geofiz* **12**, 1856 (1963).
11. Pond, S. & Stewart, R. W. Measurement of statistical characteristics of small-scale turbulence. *Izv. Akad. Nauk SSSR, Ser. Geofiz* **1**, 914 (1965).
12. Yaglom, A. M. The influence of fluctuations in energy dissipation on the shape of turbulent characteristics in the inertial interval. *Sov. Phys. Dokl.* **11** (1966).
13. Monin, A. S. & Yaglom, A. M. *Statistical fluid mechanics, volume II: mechanics of turbulence*, vol. 2, chap. 8 (Courier Corporation, 2013).

14. Frisch, U., Sulem, P.-L. & Nelkin, M. A simple dynamical model of intermittent fully developed turbulence. *J. Fluid Mech.* **87**, 719–736 (1978).
15. Benzi, R., Paladin, G., Parisi, G. & Vulpiani, A. On the multifractal nature of fully developed turbulence and chaotic systems. *J. Phys. A: Math. Gen.* **17**, 3521 (1984).
16. Schertzer, D. & Lovejoy, S. Elliptical turbulence in the atmosphere. In *Symposium on Turbulent Shear Flows, 4 th, Karlsruhe, West Germany*, 11 (1984).
17. Meneveau, C. & Sreenivasan, K. Simple multifractal cascade model for fully developed turbulence. *Phys. review letters* **59**, 1424 (1987).
18. Schertzer, D. & Lovejoy, S. Physical modelling and analysis of rain and clouds by anisotropic scaling and multiplicative processes. *J. Geophys. Res.* **92**, 9693–9714 (1987).
19. She, Z.-S. & Leveque, E. Universal scaling laws in fully developed turbulence. *Phys. review letters* **72**, 336 (1994).
20. Schmitt, F. G. & Huang, Y. *Homogeneous turbulence and intermittency*, 12–40 (Cambridge University Press, 2016).
21. Chigirinskaya, Y., Schertzer, D., Lovejoy, S., Lazarev, A. & Ordanovich, A. Unified multifractal atmospheric dynamics tested in the tropics: part I, horizontal scaling and self criticality. *Nonlinear Process. Geophys.* **1**, 105–114, DOI: [10.5194/npg-1-105-1994](https://doi.org/10.5194/npg-1-105-1994) (1994).
22. Lazarev, A., Schertzer, D., Lovejoy, S. & Chigirinskaya, Y. Unified multifractal atmospheric dynamics tested in the tropics: part II, vertical scaling and generalized scale invariance. *Nonlinear Process. Geophys.* **1**, 115–123, DOI: [10.5194/npg-1-115-1994](https://doi.org/10.5194/npg-1-115-1994) (1994).
23. Samorodnitsky, G. & Taqqu, M. S. *Non-Gaussian Stable Processes: Stochastic Models with Infinite Variance*. Chapman Hall, Lond. (1994).
24. Schmitt, F. & Marsan, D. Stochastic equations generating continuous multiplicative cascades. *The Eur. Phys. J. B-Condensed Matter Complex Syst.* **20**, 3–6 (2001).
25. Goto, Y., Yasuda, I. & Nagasawa, M. Comparison of Turbulence Intensity from CTD-Attached and Free-Fall Microstructure Profilers. *J. Atmospheric Ocean. Technol.* **35**, 147–162, DOI: [10.1175/JTECH-D-17-0069.1](https://doi.org/10.1175/JTECH-D-17-0069.1) (2018).
26. Batchelor, G. K. Small-scale variation of convected quantities like temperature in turbulent fluid Part 1. General discussion and the case of small conductivity. *J. Fluid Mech.* **5**, 113–133, DOI: [10.1017/S002211205900009X](https://doi.org/10.1017/S002211205900009X) (1959).
27. Ruddick, B., Anis, A. & Thompson, K. Maximum Likelihood Spectral Fitting: The Batchelor Spectrum. *J. Atmospheric Ocean. Technol.* **17**, 1541–1555 (2000).
28. Kraichnan, R. H. Small-scale structure of a scalar field convected by turbulence. *The Phys. Fluids* **11**, 945–953 (1968).
29. Goto, Y., Yasuda, I. & Nagasawa, M. Turbulence Estimation Using Fast-Response Thermistors Attached to a Free-Fall Vertical Microstructure Profiler. *J. Atmospheric Ocean. Technol.* **33**, 2065–2078, DOI: [10.1175/JTECH-D-15-0220.1](https://doi.org/10.1175/JTECH-D-15-0220.1) (2016).
30. Roget, E., Lozovatsky, I., Sanchez, X. & Figueroa, M. Microstructure measurements in natural waters: Methodology and applications. *Prog. Oceanogr.* **70**, 126–148 (2006).
31. Peterson, A. K. & Fer, I. Dissipation measurements using temperature microstructure from an underwater glider. *Methods Oceanogr.* **10**, 44–69 (2014).
32. Antonia, R. & Orlandi, P. On the Batchelor constant in decaying isotropic turbulence. *Phys. Fluids* **15**, 2084–2086 (2003).
33. Bogucki, D., Domaradzki, J. A. & Yeung, P. Direct numerical simulations of passive scalars with $Pr > 1$ advected by turbulent flow. *J. Fluid Mech.* **343**, 111–130 (1997).
34. Bogucki, D., Luo, H. & Domaradzki, J. Experimental evidence of the Kraichnan scalar spectrum at high reynolds numbers. *J. Phys. Oceanogr.* **42**, 1717–1728 (2012).
35. Sanchez, X., Roget, E., Planella, J. & Forcat, F. Small-scale spectrum of a scalar field in water: the Batchelor and Kraichnan models. *J. Phys. Oceanogr.* **41**, 2155–2167 (2011).
36. Lovejoy, S. & Schertzer, D. *The Weather and Climate: Emergent Laws and Multifractal Cascades* (Cambridge University Press, 2013).
37. Gires, A., Tchiguirinskaia, I., Schertzer, D. & Lovejoy, S. Development and analysis of a simple model to represent the zero rainfall in a universal multifractal framework. *Nonlinear Process. Geophys.* **20**, 343–356 (2013).
38. Parisi, G. & Frish, U. *A multifractal model of intermittency*, 111–114 (Elsevier North Holland, New-York, 1985).

39. Schertzer, D. & Lovejoy, S. Universal multifractals do exist! *J. Appl. Meteorol.* **36**, 1296–1303 (1997).
40. Schmitt, F. G. Modeling of Turbulent Intermittency: Multifractal Stochastic Processes and Their Simulation. In Seuront, L. & Strutton, P. G. (eds.) *Handbook of scaling methods in aquatic ecology: measurement, analysis, simulation*, chap. 29, 453–468 (CRC Press, 2003).
41. Misiorek, A. & Weron, R. *Heavy-Tailed Distributions in VaR Calculations*, 1025–1059 (Springer Berlin Heidelberg, Berlin, Heidelberg, 2012).

Acknowledgements

Helpful comments received from Yutaka Yoshikawa (Kyoto University) are highly appreciated. This work was partially supported by a Grant-in-Aid for Scientific Research on Innovative Areas (MEXT KAKENHI-JP15H05817/JP15H05819). We also thank the members of the project for their valuable discussions on the concept and method. We would like to thank Editage for English language editing. All numerical simulations were performed on the JAMSTEC Data Analyzer (DA) system. The ocean turbulence dataset is under preparation for public release by the Atmosphere and Ocean Research Institute, University of Tokyo.

Author contributions

SM and SO posed the main problem. IY compiled the observational data. IY, SK, SM, and SO helped formulate the hypothesis. NS proposed the method, performed the statistical analyses, and prepared the manuscript with contributions from all co-authors.

Competing interests

The authors declare no competing interests.